buildings

MDPI

Article

Damage Assessment of RC Beam–Column Joints via Digital Image Correlation and Fractal Dimension Analysis

Qirui Zhong [1], Xiang Wang [1,*], Zeyu Chen [2], Bo Cui [2] and Xiaolei Han [2]

[1] School of Civil Engineering, Sun Yat-sen University, Zhuhai 519082, China; zhongqr5@mail2.sysu.edu.cn
[2] School of Civil Engineering and Transportation, South China University of Technology, Guangzhou 510641, China; ctchenzeyu@mail.scut.edu.cn (Z.C.); 202421008624@mail.scut.edu.cn (B.C.); xlhan@scut.edu.cn (X.H.)
* Correspondence: wangxiang5@mail.sysu.edu.cn

Abstract

Beam–column joints are critical elements in reinforced concrete (RC) frame structures. They are subjected to complicated load mechanisms in the event of earthquakes, which often leads to non-ductile damage in the form of shear cracking failure and concrete spalling. With recent advances in computer vision techniques, an image-based methodology is implemented for effectively assessing the seismic damage of RC beam–column joints. Specifically, this study integrates digital image correlation (DIC)-derived strain fields with microplane damage theory to identify concrete surface damage, and subsequently, fractal dimension analysis is employed to quantitatively evaluate the damage metric. The proposed image-based analysis procedures are implemented to investigate the damage evolution of six full-scale RC beam–column joints subjected to quasi-static loading tests. The damage results derived using fractal dimension analysis are compared with those computed using conventional mechanics-based damage models. It is observed that the fractal-based damage index of the RC joints agrees reasonably well with the stiffness-based damage index. The damage curves reveal that the DIC-assisted fractal dimension analysis provides an effective means for automated identification of the surface damage pattern as well as damage progression of RC beam–column joints under seismic loading or other complex loading scenarios.

Keywords: reinforced concrete; beam–column joints; damage assessment; digital image correlation; fractal dimension; seismic behavior

1. Introduction

Beam–column joints are critical components of reinforced concrete (RC) frame structures. They are designed to transfer loads between the connected frame members and ensure the overall integrity of the structural system. In the event of an earthquake, beam–column joints of an RC structure are often subjected to complicated load mechanisms as a result of combined axial-shear-flexural actions imposed by the adjoining frame members (e.g., beams and columns). Past earthquakes have revealed that RC beam–column joints are vulnerable to non-ductile damage in the form of shear cracking, concrete core crushing, and bond strength deterioration, all of which may lead to severe damage to the structural system or even collapse [1–5]. In this regard, researchers have conducted extensive experimental studies to develop enhanced design strategies for improving the seismic performance of RC beam–column joints (e.g., [6–9]).

Despite these research efforts, the evaluation of seismic damage of RC beam–column joints remains challenging due to the complicated loading mechanisms during earthquakes.

Check for updates

Academic Editor: Weijing Zhang

Received: 24 May 2026
Revised: 25 June 2026
Accepted: 26 June 2026
Published: 28 June 2026

Copyright: © 2026 by the authors. Licensee MDPI, Basel, Switzerland. This article is an open access article distributed under the terms and conditions of the Creative Commons Attribution (CC BY) license.

Amid recent progress in non-destructive monitoring, vision-based techniques have emerged as an effective means for structural damage identification. Early implementations of vision-based structural damage identification primarily focus on detecting surface defects (e.g., cracks, spalling) of RC structures (e.g., [10–13]). These approaches rely heavily on image processing algorithms (e.g., thresholding, edge detection, morphological operations) for image feature or pattern detection, which often require ad-hoc parameter calibration for achieving optimal damage identification results, thereby restricting the generalizability of such approaches. Benefiting from the rapid progress of artificial intelligence in recent decades, image-based learning methods have substantially enhanced the accuracy and efficiency of structural damage detection [14,15], and therefore have been applied in a variety of real-world applications, such as post-hazard damage assessment (e.g., [16–18]) and operational condition monitoring (e.g., [19–21]). Although image-based learning techniques provide valuable insights into qualitative structural damage assessment (e.g., detection, classification, and localization), information relevant to the physical mechanism or quantitative evaluation of the structural damage remains insufficient.

Complementing the limitations associated with image-based learning techniques, Digital Image Correlation (DIC) has gained increasing popularity in structural experiments, since it enables full-field, non-contact measurements of the physical behavior (e.g., deformation, strain) of structural components in response to external loads [19–21]. In this regard, this technique has been extensively utilized for experimental investigation on the mechanical behavior of RC structures at various scales, including the material, interfacial bonding, and component testing (e.g., [22–24]). Furthermore, researchers have also developed sophisticated algorithms for detecting the crack behavior of RC structures using DIC analysis (e.g., [25–27]). Since crack propagation is indicative of physical structural damage, a novel computer vision technique, namely, fractal dimension analysis, is employed to quantitatively evaluate the damage of RC structures [28]. Its capability for analyzing complex geometric shapes renders it an effective tool for quantitative damage assessments of RC structures. Recently, fractal dimension analysis has been implemented for evaluating the structural damage of beams, columns, and shear walls using the crack characteristics of RC specimens (e.g., [29–31]). However, the effectiveness of this method for characterizing the physical mechanisms of RC structures under complex loading scenarios (e.g., combined axial and shear loading) requires further validation.

To this end, this study proposes an image-based methodology for quantitative analysis of the seismic damage of RC beam–column joints. Notably, the RC joints are often characterized by combined axial–shear–flexural loads under lateral seismic loads, which often lead to complicated damage patterns in the form of diagonal cracks and compression struts. Displacement and strain fields of the joints under seismic loading are extracted using speckle images recorded by a stereo DIC system, and subsequently, fractal dimension analysis is conducted to detect the surface crack pattern and track the damage progression of the joints. The effectiveness of the image-based damage analysis procedures is validated using quasi-static tests of six full-scale RC beam–column subassemblies. Comparison of the image-based damage assessment results with the conventional seismic damage indices reveals that the fractal-based damage of the RC joints correlates well with the stiffness-based damage metric. The damage curves confirm that the DIC-assisted fractal dimension analysis provides a promising means for efficiently evaluating the surface damage pattern and damage progression of RC beam–column joints under seismic loads. It is noted that the validity of the proposed damage assessment methodology is limited to RC beam–column joints dominated by shear failure. Therefore, future validation studies of other RC elements (e.g., columns, walls) are encouraged to extend the applicability of the proposed image-based analysis procedures.

2. Image-Based Damage Assessment Procedures

As shown in Figure 1, the proposed image-based analysis procedures for RC beam–column joint damage assessment are divided into four steps: (1) speckle pattern design and camera calibration, (2) joint strain field calculation via digital image correlation (DIC) analysis, (3) strain-based joint damage quantification via the microplane damage theory [32], and (4) joint damage assessment via fractal dimension analysis. The tasks associated with the first step, namely, speckle pattern design and camera calibration, are performed prior to the test phase. In the second step, the speckle images obtained during the quasi-static tests are analyzed using the DIC technique to extract the displacement and strain fields of the beam–column joints. In the third step, the microplane damage model [32] is employed to calculate strain tensor fields and binary damage fields of the beam–column joints. In the last step, the box-counting method is adopted for processing the binary damage field and evaluating the fractal-based damage index of the beam–column joints. In this study, the displacement and strain fields of the beam–column joints are computed using the commercial software VIC-3D (version 9) [33], and the damage analysis procedures in the subsequent steps are implemented in MATLAB (version 24.1) [34]. The implementation details of key procedures are elaborated in the remainder of this section.

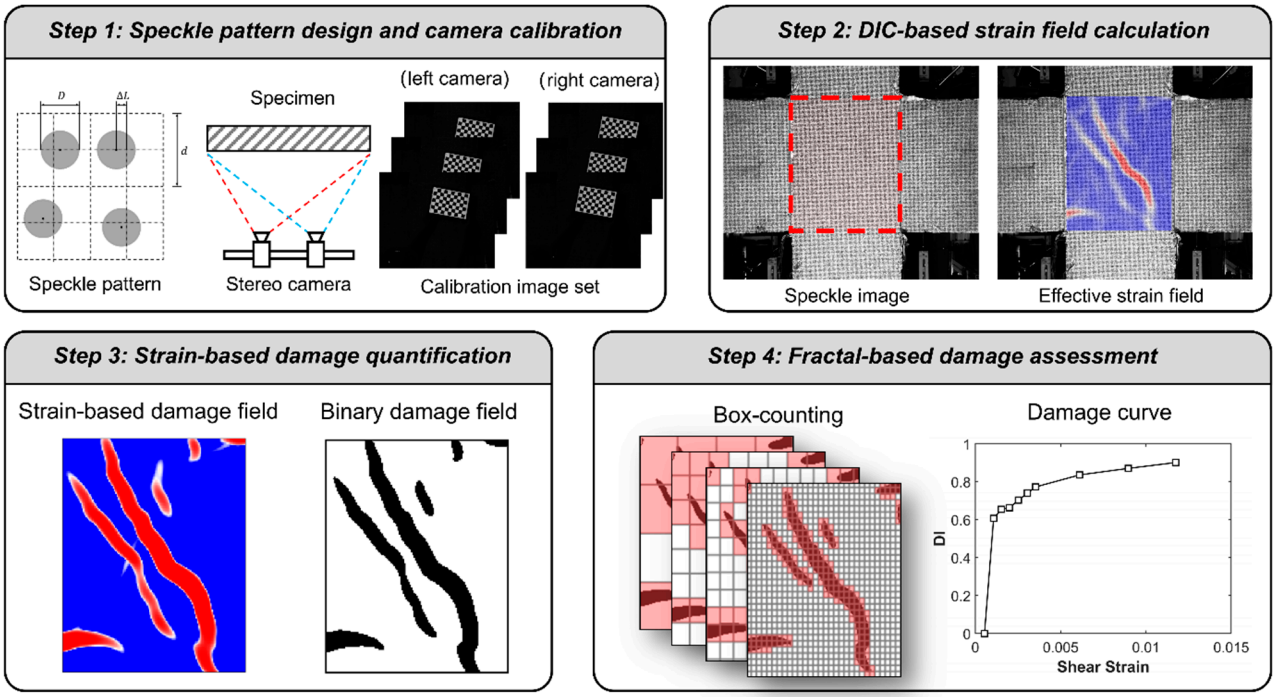

Figure 1. Overview of the image-based methodology for RC beam–column joint damage assessment.

2.1. Speckle Pattern Parameters

Since displacement and strain fields extracted using DIC are adopted for beam–column joint damage assessment, it is essential to ensure the quality of the DIC speckle pattern as well as the precision of displacement measurements [35–37]. As illustrated in Figure 2b, key parameters associated with the DIC speckle patterns involve the speckle diameter, density, and positional variation. Validation studies were conducted in the pretest phase to determine a set of optimized parameters for the speckle pattern in support of the image quality for DIC analysis of the beam–column joint. The speckle diameter D is determined using the pixel coverage criteria with a minimum size of five pixels, and therefore a diameter of 2 mm is adopted. The speckle density, which is referred to as the ratio between the area covered by speckles and the total area of the given region of interest (ROI), is often

recommended to be higher than 60% in practice. Moreover, the positional variation of the speckle is controlled by the normalized offset ΔL, which is the ratio between the speckle offset from the grid line center and the speckle radius $D/2$. The presence of positional variation for the speckles is intended to improve the stability of DIC analysis results via the introduction of randomness into the speckle pattern. Specifically, the speckle parameters are determined by evaluating the mean intensity gradient (MIG) and conducting zero-strain baseline tests on the stationary image dataset collected during the pretest stage. The adopted parameters, namely, a speckle density of 75% and positional variation of 20%, yield an optimal error metric such that the measured displacements are minimized.

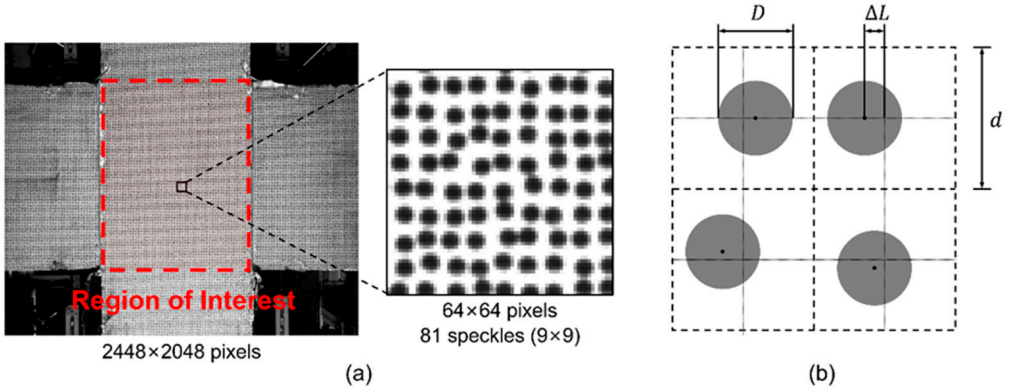

Figure 2. DIC speckle pattern applied on the beam–column joint: (**a**) full-frame camera view and close-up view of the speckle pattern; (**b**) parameters associated with the speckle pattern (notes: D: speckle diameter, d: speckle spacing, ΔL: speckle offset).

2.2. Stereo Camera Calibration

Stereo camera calibration is the process of estimating the intrinsic and extrinsic parameters of each camera in the stereo system. The intrinsic parameters are used to remove lens-induced distortion effects (e.g., barrel distortion, tangential distortion) from the raw images, whereas the extrinsic parameters refer to the positional information of the cameras (e.g., camera orientation, baseline, etc.), which are essential for computing the disparity (or depth) of the image pairs. For this exercise, a 12 × 9 checkerboard target with a tile size of 30 mm is used for the stereo camera calibration, and the parameters of the stereo system are determined using the stereo camera calibration app in the MATLAB computer vision toolbox [34]. Interested readers are referred to the MATLAB user manual for additional details regarding the stereo camera calibration procedures [34].

2.3. Strain Field Calculation via DIC

DIC is a non-contact optical measurement technique that measures full-field deformation and strain fields of a target surface by tracking the evolution of its speckle pattern. In the DIC analysis procedures, an image frame is segmented into an array of square-shaped subsets with a uniform size, and the displacements of each subset are subsequently determined by registering the deformed subset with the highest correlation to the reference (undeformed) subset [35]. In this exercise, the displacement and strain fields of the beam–column joints are computed using the commercial software VIC-3D [33]. According to validation against displacement data collected by analog sensors, the subset size and step size are taken as 20 and 5 pixels, respectively. Importantly, the step size of 5 pixels as employed in the DIC analysis (Step 2, Figure 1) also serves to downsample the original image resolution for the subsequent damage quantification analysis (Steps 3 and 4, Figure 1). For instance, with an ROI of 900 × 1100 pixels, a step size of 5 pixels reduces

the image resolution to 180 × 220 pixels for the strain-based damage quantification and fractal analysis.

The DIC analysis aims to obtain the maximum principal strain field of the beam–column joint, which is implemented as a three-step procedure as schematically illustrated in Figure 3. In the first step, the in-plane displacement components of the beam–column joint, namely, $u(x, y)$ and $v(x, y)$, are extracted from a pair of DIC speckle images. Subsequently, the displacement gradient tensor ∇U is calculated using the displacement fields obtained in the first step, which is defined as:

$$\nabla U = \begin{pmatrix} \frac{\partial u}{\partial x} & \frac{\partial u}{\partial y} \\ \frac{\partial v}{\partial x} & \frac{\partial v}{\partial y} \end{pmatrix} \tag{1}$$

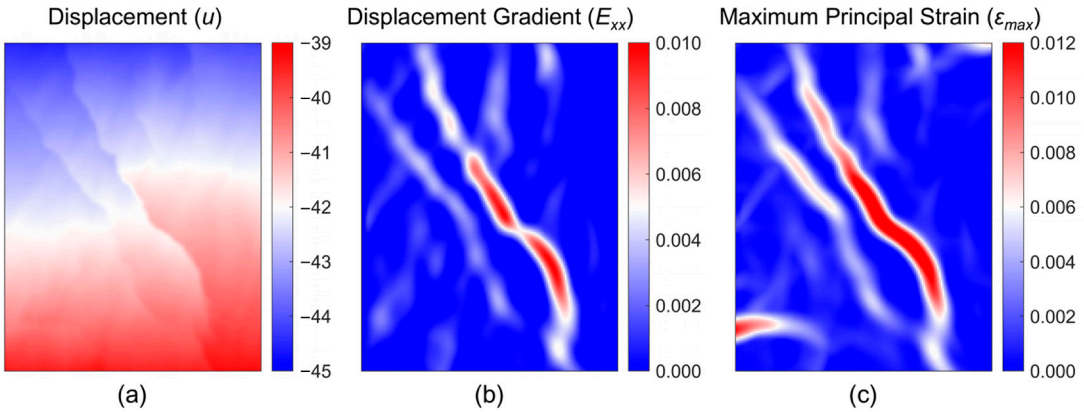

Figure 3. Digital image correlation analysis results of the beam–column joint: (**a**) displacement field (units in pixel), (**b**) displacement gradient field, and (**c**) maximum principal strain field.

Since displacement gradients are dimensionless quantities, they can be estimated directly using the displacement fields measured under the pixel coordinates regardless of their metric units (e.g., mm). In this study, the displacement gradients are estimated using the central difference method with a step size of five pixels (e.g., $\frac{\partial u}{\partial x} = \frac{u(x+\Delta x,\, y)-u(x-\Delta x,\, y)}{2\Delta x}$). In the last step, the Green–Lagrange strains E_{xx}, E_{yy}, and E_{xy} of the beam–column joint are computed according to the following equations:

$$E_{xx} = \frac{\partial u}{\partial x} + \frac{1}{2}\left[\left(\frac{\partial u}{\partial x}\right)^2 + \left(\frac{\partial v}{\partial x}\right)^2\right] \tag{2}$$

$$E_{yy} = \frac{\partial v}{\partial y} + \frac{1}{2}\left[\left(\frac{\partial u}{\partial y}\right)^2 + \left(\frac{\partial v}{\partial y}\right)^2\right] \tag{3}$$

$$E_{xy} = \frac{1}{2}\left[\frac{\partial u}{\partial y} + \frac{\partial v}{\partial x} + \frac{\partial u}{\partial x}\frac{\partial u}{\partial y} + \frac{\partial v}{\partial x}\frac{\partial v}{\partial y}\right] \tag{4}$$

Given the Green–Lagrange strains, the maximum principal strain ε_1 is derived via strain tensor eigen analysis, which is given as:

$$\varepsilon_1 = \frac{E_{xx} + E_{yy}}{2} + \sqrt{\frac{\left(E_{xx} - E_{yy}\right)^2}{4} + {E_{xy}}^2} \tag{5}$$

2.4. Strain-Based Damage Quantification

In the damage quantification step, the microplane damage theory [32] is adopted to convert the strain field of the beam–column joint into a simple scalar damage field

(Figure 4). In this regard, a strain tensor-based damage metric ω is defined as a function of the equivalent strain κ, which is taken as the maximum principal strain attained during the loading history [38]. This ensures that the damage metric ω increases monotonically during the loading history. Specifically, the strain tensor-based damage of the beam–column joint is computed using the exponential damage law, which is expressed as:

$$\omega(\kappa) = 1 - \frac{\varepsilon_0}{\kappa}\exp\left(-\frac{\kappa - \varepsilon_0}{\varepsilon_f - \varepsilon_0}\right) \tag{6}$$

where ε_0 denotes the strain associated with the initial inelasticity, and ε_f denotes the strain associated with damage initiation. Absent concrete material test data, the recommended ε_0 range of 0.002~0.0025 for normal-strength concrete is considered in this study, and ε_f is assumed to be larger than ε_0 by a constant difference of 0.001 [38]. As shown in Figure 5, the strain tensor-based damage $\omega(\kappa)$ is 0 when the equivalent strain κ equals ε_0 and approaches 1 as the equivalent strain κ becomes sufficiently large (>0.006). Additionally, the increase in ε_0 appears to reduce damage when the equivalent strain κ (i.e., maximum principal strain) remains smaller than 0.004. Therefore, the initial inelasticity strain ε_0 is a critical parameter for evaluating early-stage damage of the beam–column joints. The effect of this parameter on the damage analysis results is discussed in the next section.

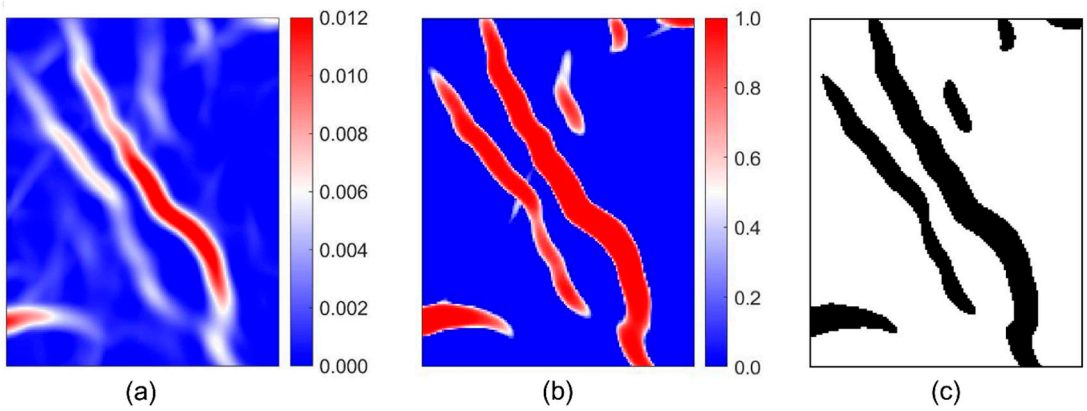

Figure 4. Damage binarization process of the RC beam–column joints: (**a**) principal strain field, (**b**) strain tensor-based damage field, and (**c**) binary damage field.

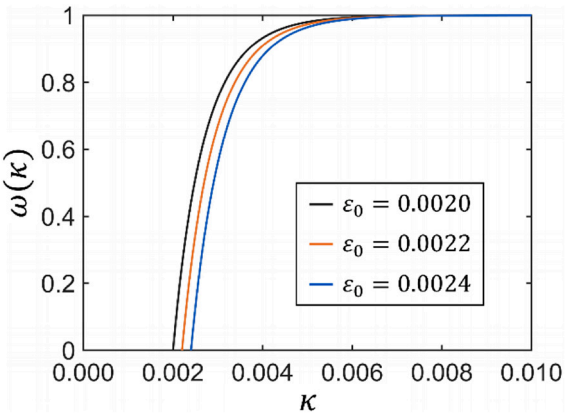

Figure 5. The effect of initial inelastic strains ε_0 on the strain-based damage $\omega(\kappa)$.

To facilitate fractal dimension analysis, a damage threshold ω_T is introduced to convert the strain-based damage field of the beam–column joint into a binary damage field. As shown in Figure 4c, image pixels with $\omega(\kappa) \geq \omega_T$ are classified as damage pixels (denoted

in black) and otherwise classified as damage-free pixels (denoted in white). According to the findings from previous studies [26,27], a ω_T value between 0.4 and 0.6 is considered reasonable for the binary damage thresholding. As demonstrated in the next section, the variation of the damage threshold may slightly modify the damage pattern of the joints, but its effect on the damage assessment results is considered inconsequential. Admittedly, the binary damage field derived using DIC strain fields may differ from the actual crack distribution of the beam–column joints observed during the tests. Nevertheless, the strain-based damage metric is indicative of regions with a high level of strain concentration and, therefore, is used equivalently as a proxy for regions with a high possibility of crack occurrence.

2.5. Fractal-Based Damage Index

Fractal dimension analysis has been widely utilized in various domains of image processing, such as pattern recognition and image segmentation, which provides a quantitative measure of the geometric complexity of an irregular object. To this end, this concept is adopted for tracking the damage evolution of the RC beam–column joints by performing fractal dimension analysis of the binary damage map as derived in the previous step. In contrast to conventional mechanics-based damage metrics in the literature (e.g., stiffness degradation, energy dissipation), fractal dimension analysis offers unique advantages in capturing the spatially heterogeneous damage by considering multiscale morphological features of the evolution of joint cracks under quasi-static loading.

Specifically, the fractal-based damage analysis consists of two main steps, namely, fractal dimension evaluation and damage index evaluation. A common approach for estimating the fractal dimension of irregular geometric objects or patterns is the box-counting algorithm [39]. According to this approach, an image is divided into a grid of boxes with a box size r, and the number of boxes covering the target object or pattern for a given box size r is denoted as $N(r)$. As the box size r approaches zero (the box becomes infinitesimally small), the fractal dimension FD can be evaluated using the following limit form:

$$FD = lim_{r \to 0} \frac{logN(r)}{log(1/r)} \tag{7}$$

Instead of directly solving the limit as given in the above equation, an alternative to numerically estimating FD is the straight-line fitting of the $N(r)$ vs. $1/r$ scatter plot on a log–log scale, and the slope of the straight line is taken as the fractal dimension FD. If the $N(r)$ vs. $1/r$ deviates from a linear trend, the box-counting method may become ineffective for fractal dimension evaluation, and alternative approaches need to be explored. As discussed in prior studies [40], the box-counting algorithm treats each damaged pixel as equal regardless of its morphological characteristics (e.g., actual width of damage), and therefore, the use of a coarse grid size is likely to amplify noise artifacts. To address this issue, a morphological image-processing step is introduced to remove isolated pixels located near the edge or between major diagonal damage patterns, as these isolated pixels are considered noise artifacts.

The process of removing isolated noise pixels is conducted using a simple thresholding procedure. The minimum distance threshold $thres_{dist}$ is used to remove pixel clusters that are close to the edge of the binary image, whereas the minimum area threshold $thres_{area}$ is used for filtering isolated pixel clusters with a sufficiently small size (see Figure 6a). For a binary damage image, morphological analysis is first performed to extract the areas, center positions, and edge distances of the connected pixel regions, which are also known as image blobs. The blob with an edge distance d less than $thres_{dist}$ or with an area smaller than $thres_{area}$ is considered as an isolated pixel cluster (noise artifacts). In this study, the

minimum distance threshold is taken as 5 pixels, and the minimum area threshold is taken as 30 pixels. Figure 6b shows the detected noise pixels of the binary damage images. The removed pixel clusters are denoted in red, whereas the black pixels indicate the preserved damage. The noise clusters located near the edge or between the diagonal damage patterns are effectively eliminated with the image blob thresholding procedure, which is intended to enhance the consistency and robustness of the fractal dimension analysis. It is noted that these pixel-based thresholds are defined by the physical dimensions of interest and the spatial resolution (mm/pixel) of the camera system. Given a spatial resolution of ~2 mm/pixel for the present study, the 5-pixel edge distance and the 30-pixel blob threshold correspond to a physical distance of ~1 cm and an area of ~1 cm^2, respectively. When applying this methodology to different camera system setups, it is recommended that these thresholds be properly adjusted according to the new spatial resolution to preserve the corresponding physical metrics.

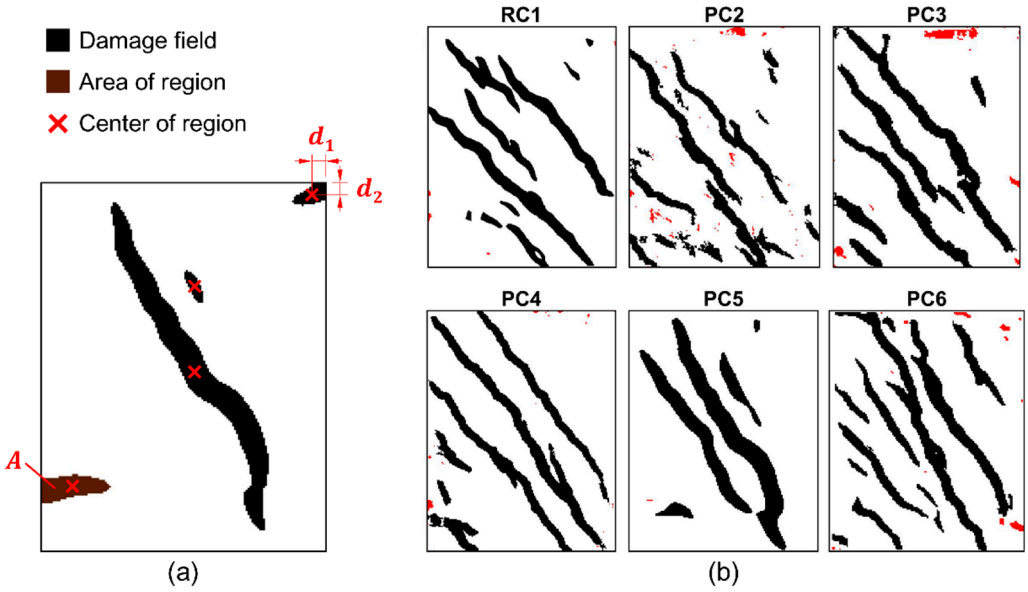

Figure 6. Binary damage image isolated pixel cluster detection: (**a**) connected region feature extraction (d_1 and d_2 represent the shortest distance between the center of region and the edge of image), and (**b**) isolated pixel clusters of the beam–column joints.

Figure 7a compares the box-counting results of a binary damage field with and without noise filtering. Note that boxes containing damaged pixels are denoted in grey, while other boxes are denoted without color. It is observed that the number count (boxes containing damage pixels) increases from 60 with a box size $R/4$ to 192 with a box size $R/16$ without noise filtering (R denotes the size of the ROI). With the implementation of noise filtering, the corresponding box numbers slightly reduce to 56 and 182, respectively. The box numbers for different box sizes are subsequently utilized for establishing a $N(r)$ vs. $1/r$ scatter plot, which is essential for numerically estimating the fractal dimension associated with each binary image. As shown in Figure 7b, the estimated fractal dimension of the binary damage field, which represents the slope of the straight line fitted using the $N(r)$ vs. $1/r$ data points, is determined as 1.652 with noise filtering in comparison to 1.644 without filtering. For the binary damage shown in Figure 7, the noise filtering of the binary damage leads to a ~5% reduction in box number count, whereas the estimated fractal dimension varies only negligibly (<1%). This is attributed to the fact that the linear regression is conducted based on box numbers on logarithmic scales.

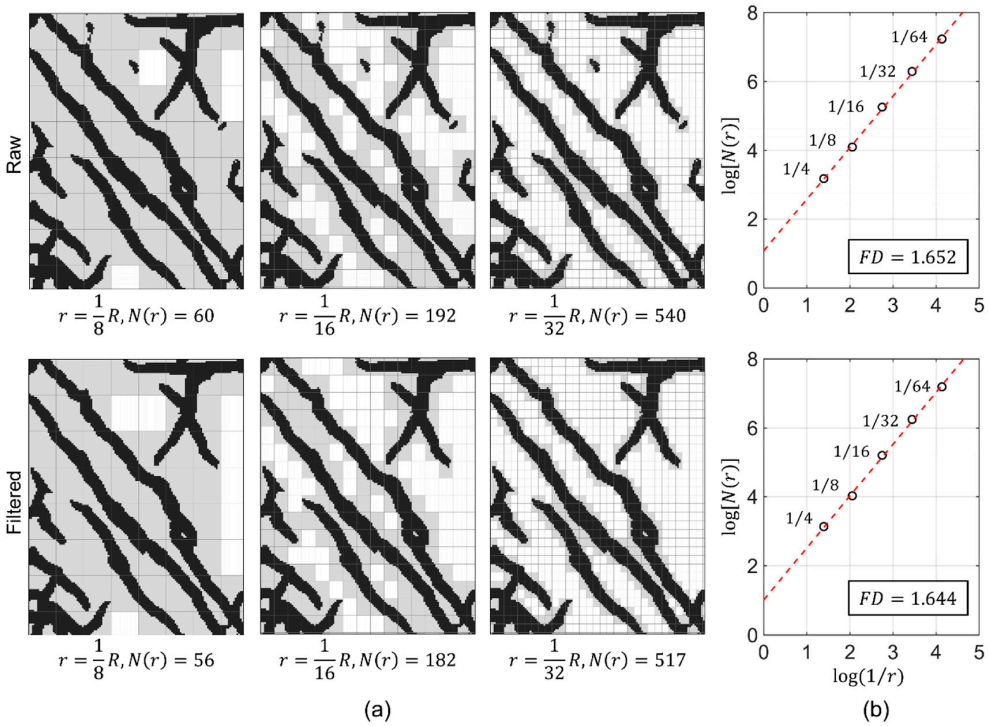

Figure 7. Box-counting method and fractal dimension calculation: (**a**) binary damage maps associated with different grid sizes, and (**b**) fractal dimension estimation by linear regression.

For quantitative assessment of structural damage from the fractal dimension perspective, Farhidzadeh et al. [41] proposed a fractal-based damage index DI_{FD}:

$$DI_{FD} = \frac{FD_i - FD_0}{2 - FD_0} \tag{8}$$

where FD_0 denotes the fractal dimension of the reference (undamaged) state, and FD_i denotes the fractal dimension of a given state i (current state). It is noted that the upper-limit fractal dimension FD of a two-dimensional shape is theoretically defined as 2, which corresponds to a complete area-filling damage pattern. As such, the upper bound of the fractal-based damage index DI_{FD} is unity by substituting the upper-bound fractal dimension of 2 into Equation (8). However, since the binary damage field (or equivalently the crack pattern) of the beam–column joint would never fill the entire joint, the fractal-based damage index as determined using Equation (8) consistently remains smaller than 1.

2.6. Limitations of the Proposed Damage Analysis Procedures

The proposed vision-based damage analysis is intended to track the damage of RC beam–column joints from the crack initiation until the onset of concrete spalling. Within this loading stage, the principal strain fields and the binarized damage strain maps correlate strongly with the physical damage of RC joints induced by the progression of surface cracks. However, following the onset of spalling that typically occurs after peak strength, the displacement and strain fields become discontinuous, rendering fractal-based damage indices evaluated from these fields ineffective. Consequently, the proposed damage analysis procedures are primarily utilized for tracking RC joint damage up to peak strength (i.e., prior to concrete spalling) and are not applicable for post-peak or ultimate failure assessment.

Furthermore, although the vision-based damage tracking and analysis procedures provide a streamlined solution for the evaluation of RC joint damage, several tuning parameters (e.g., the DIC subset size, inelastic strain threshold, and morphological noise

filter) require careful pre-test calibration. A thorough understanding of these constraints is essential for properly implementing this methodology in future applications.

3. Reinforced Concrete Beam–Column Subassembly Tests

3.1. Overview of the Test Program

An experimental effort consisting of quasi-static testing of six beam–column subassemblies was conducted to investigate the seismic behavior of a novel joint detailing strategy for connecting precast columns and cast-in-place beams in RC frame structures [42]. As summarized in Table 1, test variables of the specimens include the axial load ratio, joint concrete strength, and joint transverse reinforcement ratio. The axial load ratio is defined as the ratio between the constant axial compression load and the nominal axial compressive capacity of the column cross-section (which is determined as the product of the concrete nominal compressive strength and the gross cross-sectional area of the column). The cast-in-place specimen (RC1) was designed as a code-conforming specimen to represent a standard interior joint of a moment-resisting RC frame. Apart from the cast-in-place specimen (RC1), all remaining five specimens (PC2–PC6) were constructed using precast columns in combination with cast-in-place beams and joints. Figure 8 outlines the geometric dimensions and reinforcement details of the test subassemblies. The beams and columns of all test specimens were constructed using identical geometric dimensions. The cross-sectional dimensions were 400 mm × 400 mm for each column and 300 mm × 500 mm for each beam. The clear height of the columns was 1050 mm, and the clear span length of the beams was 1550 mm. Additionally, each beam–column joint had a dimension of 400 mm (width) × 500 mm (height). Interested readers are referred to Chen et al. [42] for additional details regarding the test program and the beam–column subassemblies.

Table 1. RC beam–column test subassemblies and the associated test variables.

Specimen Name	Design Axial Ratio	Concrete Grade (Beam and Joint)	Joint Transverse Reinforcement Plan	Joint Transverse Reinforcement Ratio (%)
RC1	0.2	C30	6@150	0.5
PC2	0.2	C40	6@150	0.5
PC3	0.2	C50	6@150	0.5
PC4	0.6	C40	6@150	0.5
PC5	0.6	C40	8@150	1.0
PC6	0.6	C40	10@150	1.5

3.2. Loading Protocol and Instrumentation

The beam–column subassembly was hinge-supported at the base of the lower column and the free ends of the beams, whereas a sliding roller support was placed on top of the upper column to decouple the vertical and horizontal movements of the column during each test (Figure 9a). These boundary conditions were imposed to replicate the inflection points (i.e., locations of zero bending moment sections), which are assumed to occur at the beam mid-spans and column mid-heights of a moment-resisting frame under lateral seismic loads. As shown in Figure 9a, the specimen was subjected to combined axial and horizontal loads using two servo-controlled hydraulic actuators. The vertical actuator was mounted at the top of the reaction frame to impose a constant vertical compression load to the top of the upper column, whereas the horizontal actuator was configured to apply lateral loads to the top of the upper column using a two-stage cyclic loading protocol in compliance with a testing protocol as stipulated by the Chinese standard specification for seismic testing (JGJ/T 101-2015) [43].

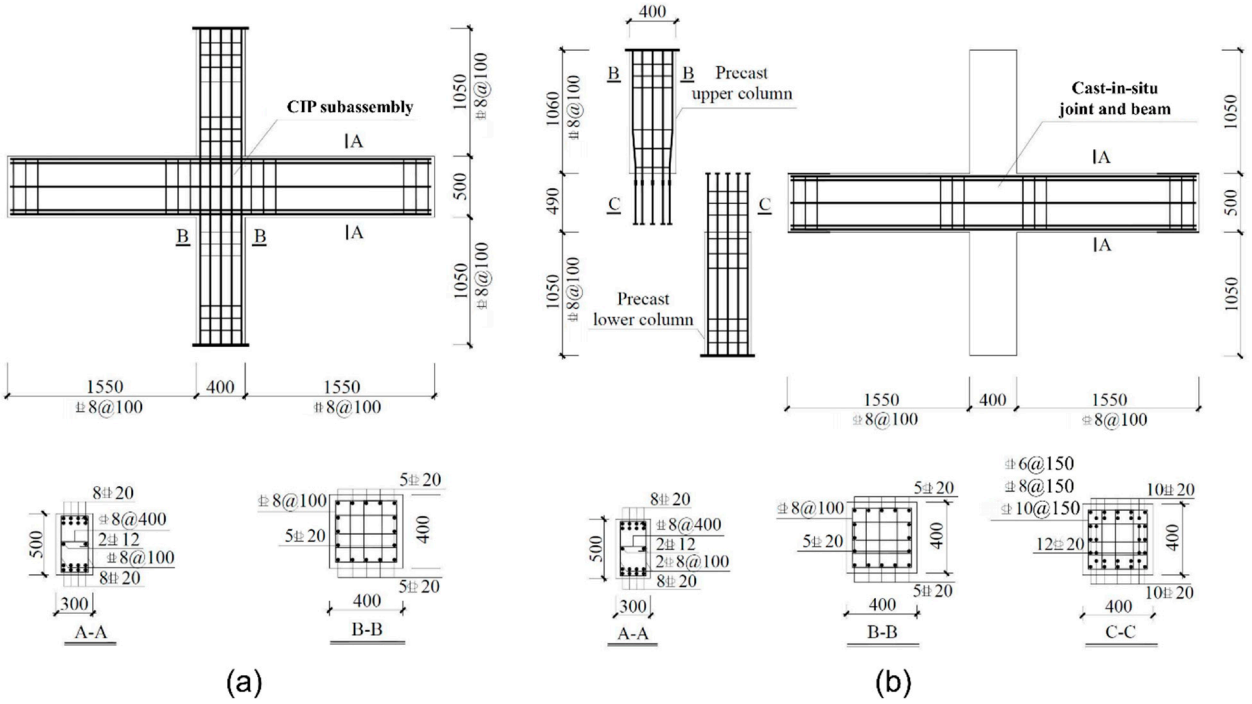

Figure 8. Geometric dimensions and reinforcement details of the beam–column subassemblies (Note: all dimensions are in millimeters, mm): (**a**) cast-in-place specimen (RC1) and (**b**) precast specimens (PC2–PC6).

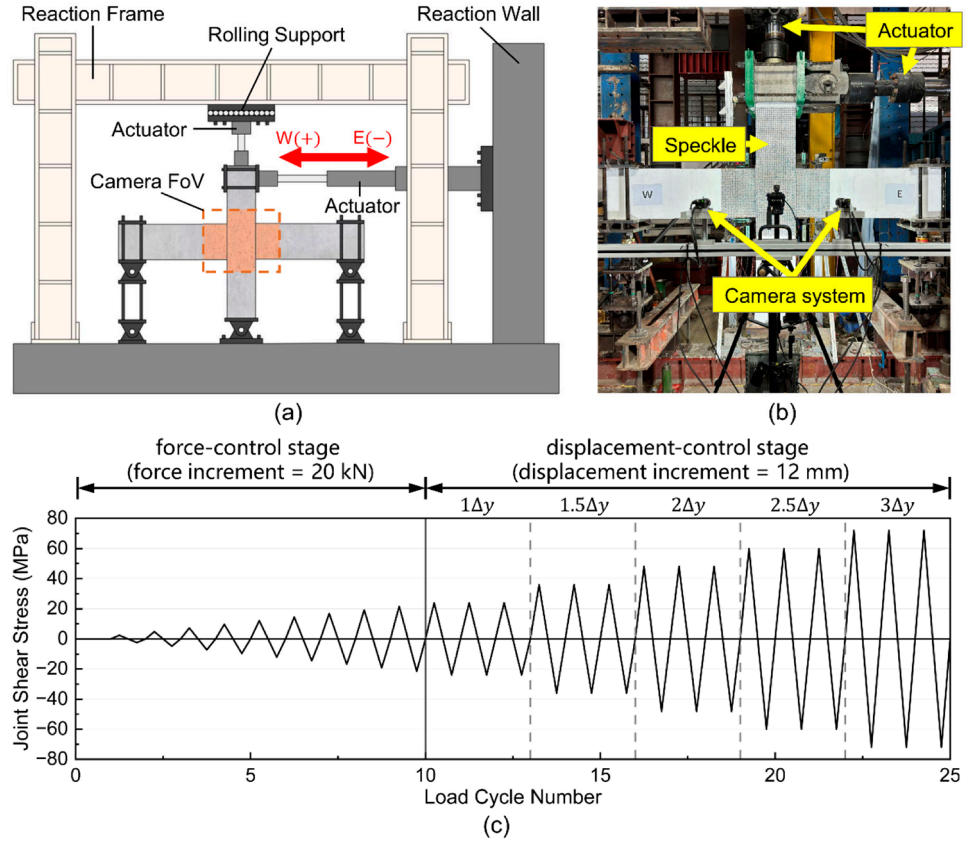

Figure 9. RC beam–column subassemblies test program: (**a**) schematic illustration of test setup (red arrow denotes the direction of loading), (**b**) stereo DIC systems and test specimen, and (**c**) loading protocol.

As shown in Figure 9c, in the force-control stage, the lateral force was applied with a single cycle per load amplitude and increased by 20 kN for each amplitude until the specimen reached a reference yield displacement of 24 mm. Subsequently, the specimen was subjected to three cycles per displacement amplitude with an increment of 12 mm for each amplitude in the displacement-control stage. The quasi-static loading test was terminated when the test specimen sustained a 15% force drop relative to its peak strength or further loading was deemed unsafe (as suggested by the JGJ/T 101-2015 testing specification [43]). It is noted that the west direction is defined as the positive direction of loading in the remainder of this paper, since it was the initial direction of loading for each test (see Figure 9a).

The horizontal force of the upper column was measured using the built-in load cell of the actuator, whereas the column displacement was measured using an external displacement transducer. Additionally, displacement transducers and strain gages were installed on the specimens to measure the local response of the specimens (e.g., joint shear deformation, joint rebar strain, etc.). Additional information regarding the instrumentation plan of the test program is available in Chen et al. [42].

3.3. Stereo DIC System

Complementing the test data measured using conventional analog sensors (e.g., displacement transducers, strain gages), a stereo DIC system was deployed to monitor full-field deformation response of the beam–column joints during the quasi-static tests. The stereo DIC system consisted of a pair of monochromatic machine-vision cameras (model #: FLIR Blackfly S BFS-U3-51S5M-C, FLIR Systems, Inc., Wilsonville, OR, USA) with a resolution of 2448 × 2048 pixels for each camera and a baseline distance of 260 mm. As shown in Figure 9b, the stereo system was mounted on a tripod leveled with the joint and placed ~2.8 m off the test specimen. Since the dimensions of the beam–column joints were 400 mm × 500 mm, the pixel resolution of the original images captured by the stereo DIC system is estimated as ~0.38 mm/pixel. Consistent with the analog data acquisition system, the images captured by the stereo camera system were sampled at a rate of 1 frame per second (1 fps) using a stand-alone laptop. The time misalignment between the image and analog datasets is determined offline by computing an autocorrelation of the column displacement measured separately by different data sources.

3.4. Seismic Response of the Beam–Column Joints

This section summarizes the seismic behavior of the RC beam–column joints under the quasi-static tests. Information provided in this section is essential for the elaboration of the image-based damage assessment methodology as presented in the following sections. Figure 10 presents the shear stress–shear strain hysteretic response of the beam–column joints. The shear stress of the joint is calculated from the measured forces of the columns and beams, whereas the joint shear strain is obtained by vision-based tracking of the in-plane displacements of the four corner points of the joint. Details regarding the data processing procedures of the joint responses are described in Chen et al. [42]. Moreover, the backbone curves, obtained by connecting the scattered data points at load reversal, are overlaid on each hysteretic plot. On the backbone curves, three representative performance states are defined: crack initiation (C), peak strength (P), and ultimate damage (U). The crack initiation state indicates the onset of diagonal cracks, and the peak strength state refers to the attainment of peak shear stress. The ultimate damage state corresponds to the shear failure of the beam–column joints since further loading is considered unsafe.

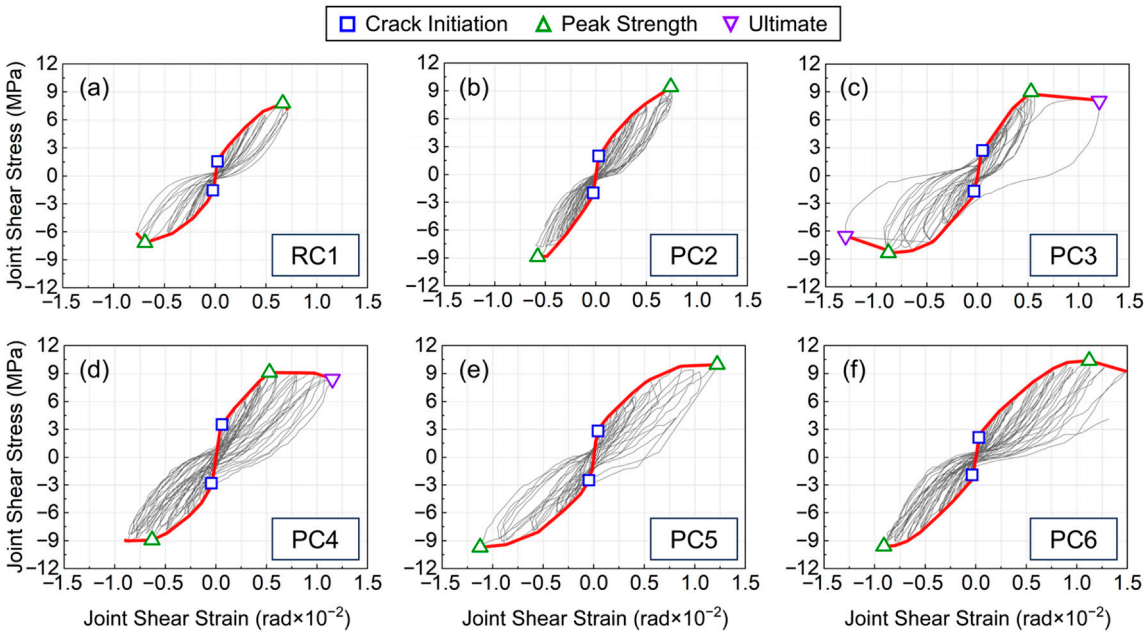

Figure 10. Shear stress–shear strain response of the beam–column joints: (**a**) RC1, (**b**) PC2, (**c**) PC3, (**d**) PC4, (**e**) PC5, and (**f**) PC6.

Table 2 summarizes the shear stress and strain of the beam–column joints at three performance states. At the crack initiation state, the stress and strain of the high axial ratio specimens (i.e., PC4, PC5, and PC6) are consistently higher than those of the low axial ratio (i.e., RC1, PC2, and PC3). This is attributed to the fact that the larger axial compression force applied on the column effectively mitigates the principal tensile stresses, thereby delaying the initiation and propagation of diagonal tensile cracks. As manifested by the severe diagonal cracks and concrete spalling, all six joints sustained shear failure at the ultimate damage state. However, the shear deformation associated with the ultimate damage state was available for only two out of the six specimens, namely, PC3 and PC4. This is attributed to the fact that the joint deformation tracking by the stereo camera system was effective only until the onset of surface concrete spalling, since the occurrence of concrete spalling prior to the ultimate damage state would render the deformation measurement unavailable. Specimens PC3 and PC4 both reached a joint shear strain as much as 0.012 rad and underwent a shear strength reduction of 10~15% at the ultimate damage state.

Table 2. Shear stress and strain associated with the representative performance states.

Performance State	Crack Initiation		Peak Strength		Ultimate	
	Stress τ_{cr} (MPa)	Strain γ_{cr} (rad)	Stress τ_p (MPa)	Strain γ_p (rad)	Stress τ_u (MPa)	Strain γ_u (rad)
RC1	1.6	0.0002	7.2	0.007	/	/
PC2	2.0	0.0002	9.0	0.006	/	/
PC3	1.7	0.0003	9.0	0.005	8.1	0.012
PC4	2.8	0.0004	9.1	0.005	8.4	0.012
PC5	2.5	0.0004	9.7	0.011	/	/
PC6	2.5	0.0003	9.5	0.009	/	/

4. Image-Based Seismic Damage Assessment of the RC Beam–Column Joints

Following the image-based damage analysis procedures as outlined in the previous section (see Figure 1), the fractal-based damage assessment results of the RC beam–column

joints under seismic loading scenarios are discussed in this section. In what follows, the damage assessment results of the beam–column joint of Specimen PC3 are elaborated to illustrate the effectiveness of the proposed methodology. Subsequently, the fractal-based damage progression of all beam–column joints is compared. Importantly, the initial inelastic strain ε_0 and binary damage threshold ω_T are two empirical parameters involved with the image-based damage analysis procedures, and therefore, this section concludes with a comprehensive investigation of their effects on the damage assessment results.

4.1. Damage Assessment Results of the Beam–Column Joints

In order to demonstrate the effectiveness of the fractal analysis in capturing the seismic damage of the beam–column joints, Figure 11 illustrates the fractal-based damage evolution of Specimen PC3 as well as the binary damage of the beam–column joint associated with five select states with evenly distributed shear strain levels (denoted as S1–S5 in the figure). It should be noted that the damage evolution curve of the joint is formed by associating the fractal-based damage indices with all load reversal points in the positive loading direction (Figure 11a,b).

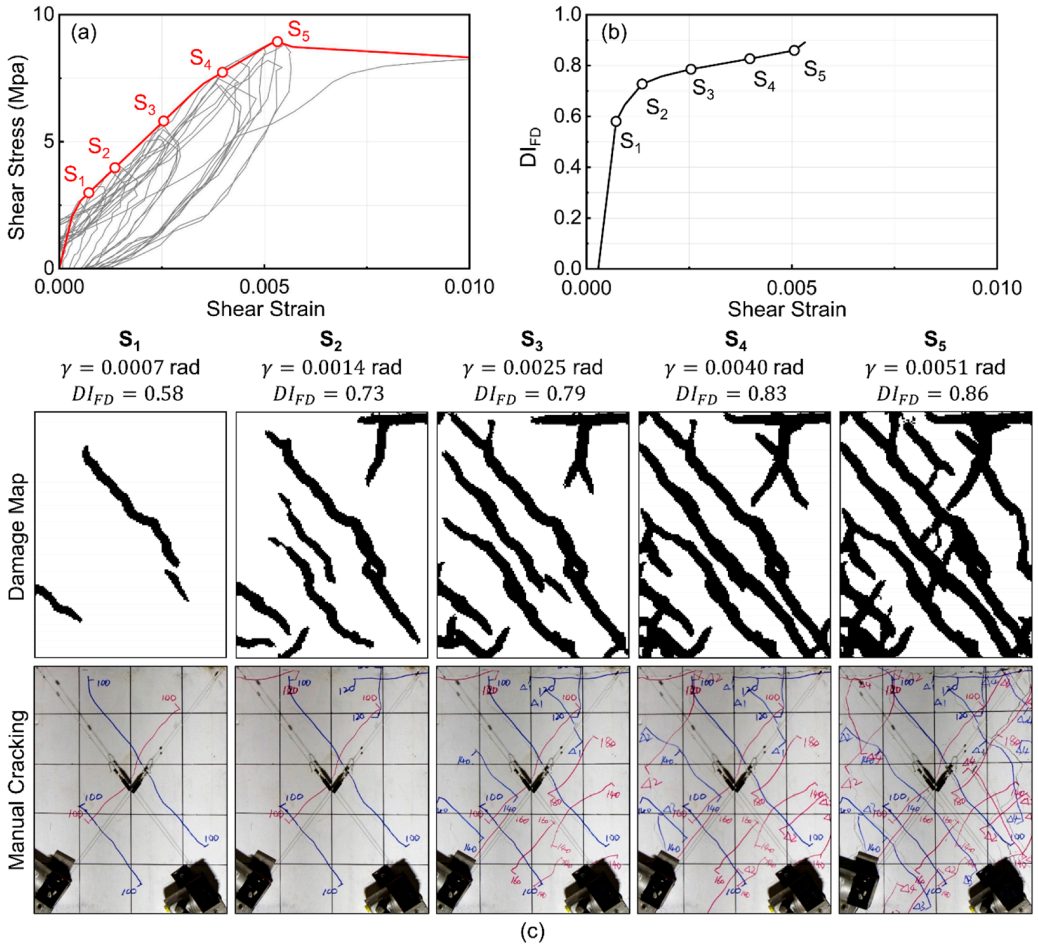

Figure 11. Fractal-based joint damage evolution of Specimen PC3: (**a**) shear stress–shear strain curve, (**b**) damage evolution curve, and (**c**) binary damage field (front side) and manually marked cracks (back side) at five select loading states (note that cracks marked in blue are formed during loading in the positive direction, and those in red are formed during loading in the negative direction).

As shown in the figure, the fractal-based damage of Specimen PC3 initiates along the main diagonal of the beam–column joint (state S1), which closely resembles the crack pattern as observed on the back side of the joint. The fractal-based damage index attains

0.58 with a shear strain demand of 0.7×10^{-3} rad. Damage in the form of a diagonal stripe continues to develop as the shear strain doubles (1.4×10^{-3} rad) at state S2, leading to an increase in the damage index to 0.73. The damage propagation reaches a stable condition as the damage index reaches 0.79 at state S3 (with a shear strain of 2.5×10^{-3} rad), since the binary damage associated with states S4 and S5 induces only a limited amount of damage in the corner regions of the joint in response to a further increase in shear strain. It is noted that state S5 corresponds to the peak strength state, and the fractal-based damage index reaches 0.86 as the shear strain achieves 5.1×10^{-3} rad. This represents merely a 10% increase in the fractal-based damage index in comparison to state S3, which indicates a much slower increase rate following the attainment of fully developed diagonal damage strips at state S3.

As shown in Figure 11c, the binary damage pattern on the front side agrees reasonably well with the crack distribution as observed on the rear side of the joint at each of the five selected loading states. Admittedly, the individual cracks identified via fractal analysis (the front side) and those marked manually (the rear side) are not perfectly coincident, owing to the highly localized nature of crack propagation. Nevertheless, the global distribution of the cracks across different loading states and the progression of the primary diagonal cracks derived by the fractal analysis closely resembles the manually marked patterns on the rear face. These results substantiate the efficacy of the image-based binary damage in assessing the overall damage evolution of RC beam–column joints under seismic loading.

Figure 12 compares the fractal-based damage evolution curves of all six beam–column joints as well as the binary damage associated with two performance states, namely, damage initiation and peak strength. It should be noted that all beam–column joints sustained severe damage at the end of the quasi-static loading tests, and therefore, image-based damage analysis is not feasible due to the occurrence of severe shear cracks and concrete spalling (Figure 12c). As such, the termination point of each damage curve reflects the peak strength state of the specimen. It is apparent that all damage curves are characterized by rapid increase at the early stage of the loading test until the damage index reaches ~0.6, with the corresponding shear strain level of $1.0\sim1.5 \times 10^{-3}$ rad, which is indicative of the fully developed diagonal damage patterns. Subsequently, the damage curves grow at a much slower rate until the specimens achieve their respective peak strength with a typical damage index range between 0.8 and 0.9. Despite the substantial differences in the initial damage patterns for different beam–column joints, the binary damage patterns of individual specimens reveal that all the joints are dominated by the presence of multiple diagonal damage strips when the peak strength is attained. These damage patterns are representative of shear-induced failure in RC components. Regardless of the variation of axial load ratio, the damage pattern of the joints under the low axial ratio (RC1, PC2, and PC3) is similar to that of the high axial ratio specimens (PC4, PC5, and PC6) at the peak strength state (refer to the middle row of Figure 12c).

4.2. Effects of Image-Based Analysis Parameters on Damage Assessment Results

As discussed in Section 2.4, the calculation of strain-based damage $\omega(\kappa)$ depends on the initial inelastic strain ε_0 and damage initiation strain ε_f. However, obtaining exact strain values relies on sophisticated material-level testing and calibration, which is often unavailable for component-level RC tests. Additionally, the damage threshold ω_T used for converting strain-based damage into binary damage is also an empirically defined parameter associated with the damage analysis procedures. Therefore, a comprehensive validation study is conducted to understand the effect of these parameters on the fractal-based damage assessment results.

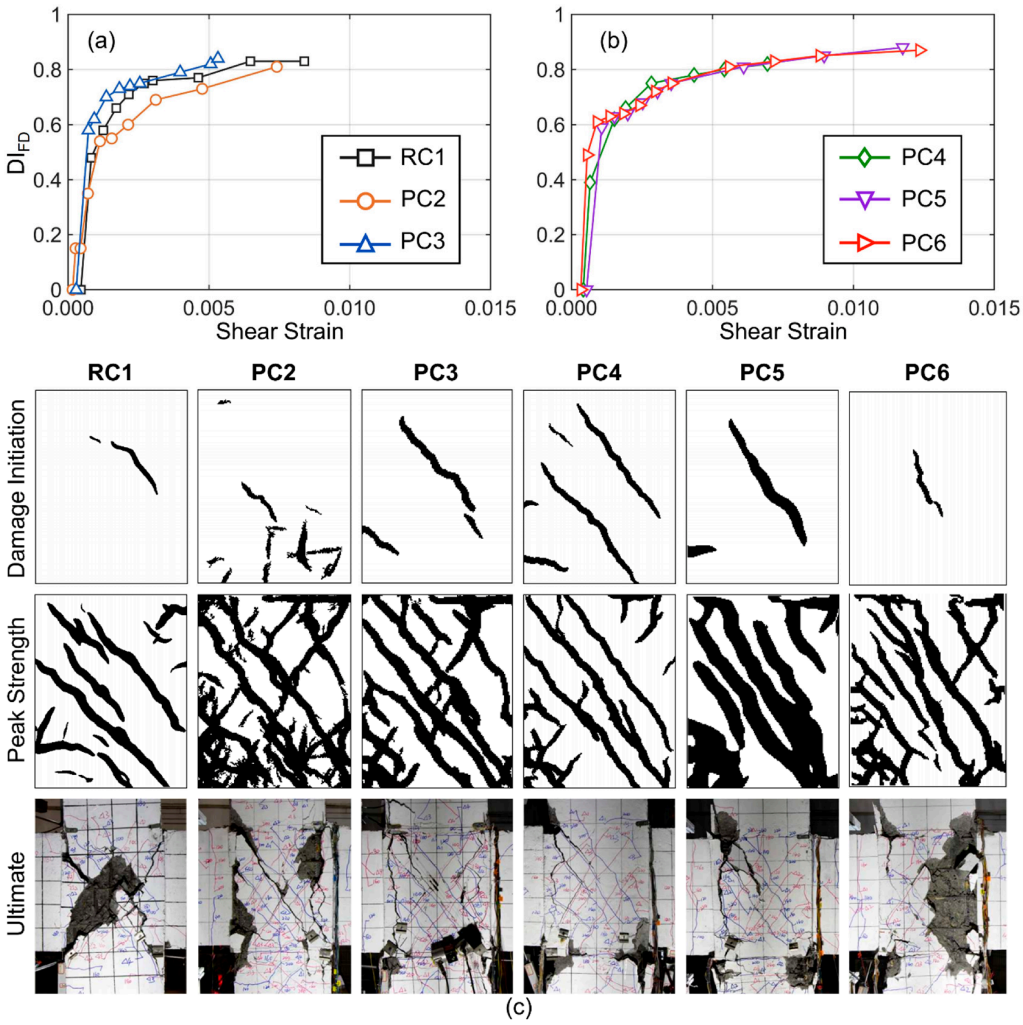

Figure 12. Comparison of fractal-based damage evolution of the beam–column joints: (**a**) damage curves of the low axial ratio specimens (RC1, PC2, and PC3), (**b**) damage curves of the high axial ratio specimens (PC4, PC5, and PC6), and (**c**) joint binary damage at different performance states.

Figure 13 compares the damage curves of Specimen RC1 as well as the binary damage associated with three representative states due to the variation of concrete inelasticity and damage strains. Since the initial inelastic strain ε_0 of 0.002~0.0025 is considered reasonable for normal-strength concrete, three ε_0 values, namely, 0.0020, 0.0022, and 0.0024, are used to investigate their effects on fractal-based damage analysis. To avoid lengthy discussions on the strain parameter selection, the damage initiation strain ε_f is simply assumed to be 0.001 greater than ε_0. Among the three representative states, states S1 and S2 correspond to the damage initiation states in the early stage of loading, since the binary damage consists of only a handful of separated damage regions, whereas state S3 indicates the peak strength state as manifested by fully developed damage patterns. As evidenced by the binary damage plots, increasing the initial inelastic strain ε_0 consistently reduces the areas of individual damage regions and smooths the edges of damage regions. Since fractal dimension is determined by the edge geometric characteristics (roughness), the use of a larger initial inelastic strain is supposed to reduce the estimated fractal dimension values. However, the estimated fractal dimension reduces insignificantly (by only 1~2%) with a strain increase from 0.002 to 0.0024 for all three states. Therefore, the comparison clearly indicates that the effect of concrete initial inelastic strain ε_0 on fractal-based damage analysis is minimal as long as they remain within the recommended range of 0.002~0.0025.

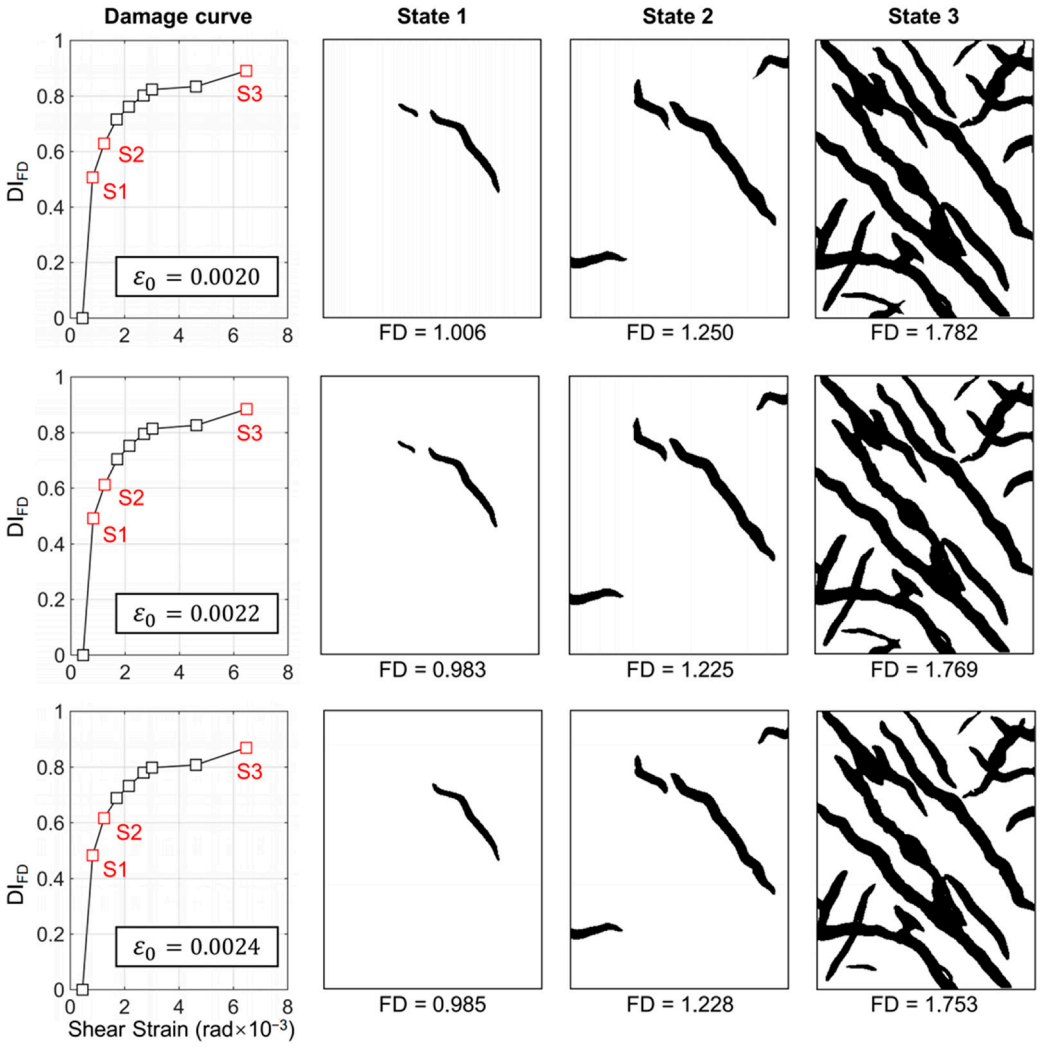

Figure 13. Damage curves of Specimen RC1 as well as the binary damage at three representative states due to the variation of concrete initial inelastic strain (Notes: FD = fractal dimension).

Likewise, the sensitivity analysis of the binary damage threshold ω_T is conducted to investigate its impact on the fractal-based damage analysis of the beam–column joints. Three distinct ω_T values, namely, 0.3, 0.5, and 0.7, are considered in the study. Figure 14 compares the damage curves of Specimen RC1 as well as the binary damage associated with three representative states due to the variation of the binary damage threshold. The selection criteria of the three representative states are identical to those of Figure 13. The binary damage plots reveal that the area of damage regions associated with each state consistently reduces as a result of the increasing damage threshold ω_T. At the initial damage state S1, the fractal dimension fluctuates in response to the decreasing damage region. This fluctuation likely arises because the limited damage may be sensitive to any subtle shape change of the damage region. As damage continues to progress in states S2 and S3, the use of a larger threshold value leads to a steady decrease in the fractal dimension. Although the estimated fractal dimension tends to be smaller with a larger damage threshold value, the estimated fractal dimension appears insensitive to the change of the threshold value, since the fluctuation remains less than 2% with the variation of the threshold within the given range (0.3~0.7). In this regard, a binary damage threshold $\omega_T = 0.5$ is adopted for the fractal-based damage analysis of the beam–column joints.

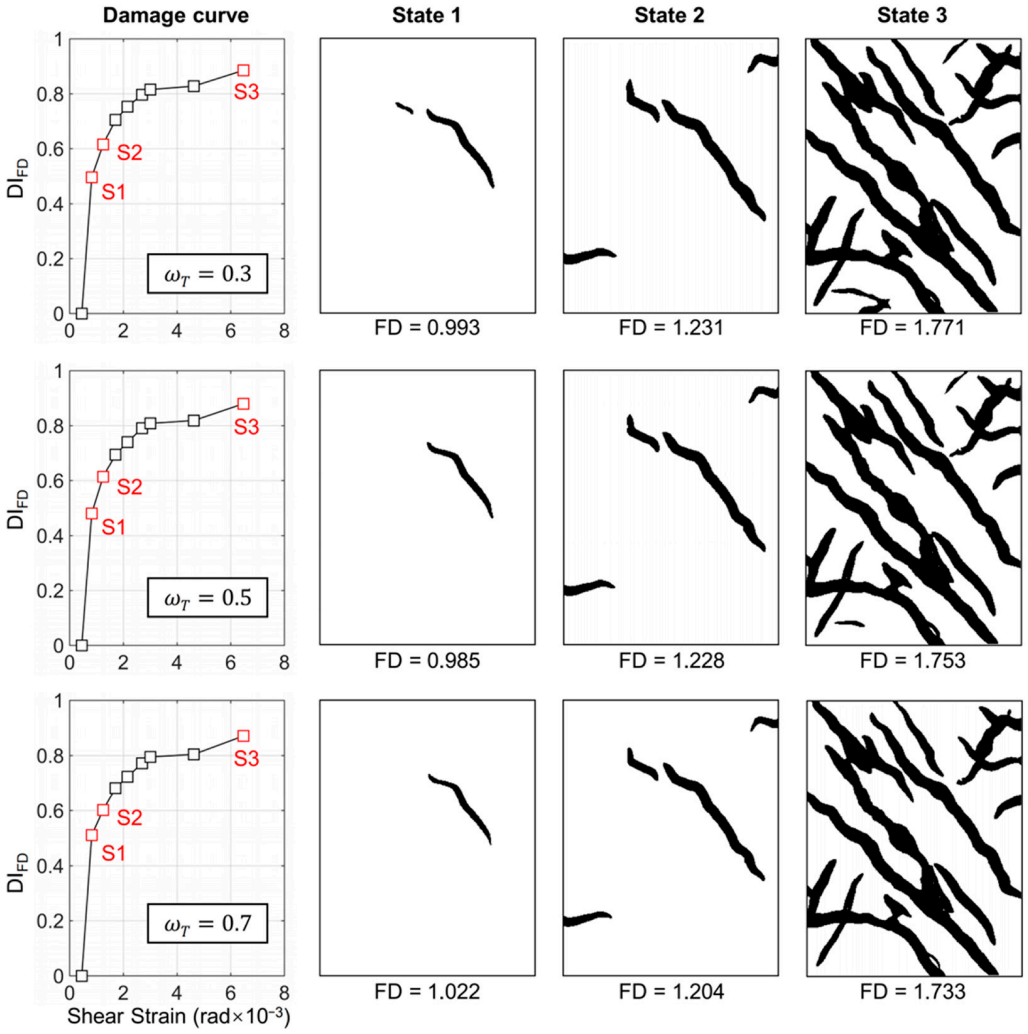

Figure 14. Damage curves of Specimen PC3 as well as the binary damage at three representative states due to the variation of binary damage threshold (Notes: FD = fractal dimension).

5. Comparison of Fractal- and Mechanics-Based Damage Metrics

Damage index (DI) has been widely adopted for evaluating the seismic damage of structural components or systems. Over the past decades, damage indices of various forms have been proposed to capture the deteriorating effects of structural behavior (e.g., strength, deformation, energy, etc.) under seismic loads [44]. Since these damage indices are derived using mechanics-based test data, they are referred to as mechanics-based damage indices in this paper. In this section, three mechanics-based damage indices commonly used in practice are utilized to evaluate the effectiveness of the proposed fractal-based damage metric on assessing the seismic damage of the beam–column joints. To provide a context for damage indices comparison, a concise description of each mechanics-based damage index is provided as follows:

(1) Stiffness-based damage index DI_K (Banon and Veneziano [45])

$$DI_K = 1 - \frac{K_i}{K_0} \tag{9}$$

where K_i represents the secant stiffness at a given state i, and K_0 represents the initial stiffness associated with the reference state. The initial stiffness K_0 of the beam–column joint refers to the secant stiffness for the crack initiation state (refer to Section 3.4). This

simple damage model characterizes the structural stiffness deterioration relative to the initial stiffness of the joint.

(2) Hysteretic energy-based damage index DI_E (Mahin and Bertero [46])

$$DI_E = \frac{E_{h,i}}{E_{h,u}} \tag{10}$$

where $E_{h,i}$ represents the cumulative hysteretic energy at a given state i, and $E_{h,u}$ is the cumulative energy dissipation capacity associated with the ultimate state. In this study, the hysteretic energy is determined numerically by summing the shear stress–shear strain hysteresis loop areas (see Figure 10). DI_E reflects the relative energy dissipation in reference to the cumulative energy dissipation capacity of the joint.

(3) Modified Park–Ang damage index DI_{mPA} [47,48]:

$$DI_{mPA} = (1-\alpha)\frac{\delta_i}{\delta_u} + \alpha\frac{E_{h,i}}{F_y\delta_u} \tag{11}$$

where δ_i and $E_{h,i}$ are the maximum joint strain achieved in the loading history and the cumulative hysteretic energy of the joint associated with a given state i, respectively; δ_u represents the ultimate (monotonic) strain capacity, and F_y is the yield strength of the specimen, which is taken as ~80% of the peak shear stress of the joint (refer to Table 2 of Section 3.4). As originally proposed by Park and Ang [47], this metric represents a linear combination of deformation- and hysteretic energy-induced damage terms; however, this damage index may exceed unity for RC structural components. In this regard, a modified Park–Ang damage index DI_{mPA} is employed by incorporating an adjustment coefficient α into Equation (11) as a controlling mechanism for the upper-bound damage index [48]. In this study, the coefficient α is determined by confining DI_{mPA} to unity at the ultimate state.

5.1. Comparison of Damage Curves

Figure 15 compares the damage curves of the RC beam–column joints as determined using the fractal- and mechanics-based damage metrics. It should be noted that the beam–column joints were subjected to different damage states at the completion of the quasi-static tests. For the purpose of evaluating the damage curves of individual beam–column joints, the ultimate state of Specimens PC3 and PC4 corresponds to the joint shear failure at the end of the test, whereas the peak strength state is considered the ultimate state for the remaining four specimens, since test data of the joint behavior was unavailable following the attainment of peak strength (refer to detailed discussions in Section 3.4). In this regard, the energy-based and modified Park–Ang damage curves (DI_E and DI_{mPA}) for Specimens RC1, PC2, PC5, and PC6 may differ from the ones evaluated using data including the failure state, whereas the fractal- and stiffness-based damage curves (DI_{FD} and DI_K) are insensitive to the prescribed ultimate state.

Regardless of the limitations associated with data completeness, the damage progression trends evaluated using different metrics are noticeably distinctive. As shown in Figure 15a, the energy-based damage curves follow an exponential form, since the damage accumulation rate continues to accelerate as a result of the rapidly growing hysteresis loops with the increasing shear strain demand. The damage accumulation rate of the modified Park–Ang curves is apparently slower than that of the energy-based curves, since the damage index is a combination of deformation- and energy-induced terms (Figure 15b). As prescribed by their underlying definitions, the energy-based and modified Park–Ang damage indices both attain unity at the ultimate state.

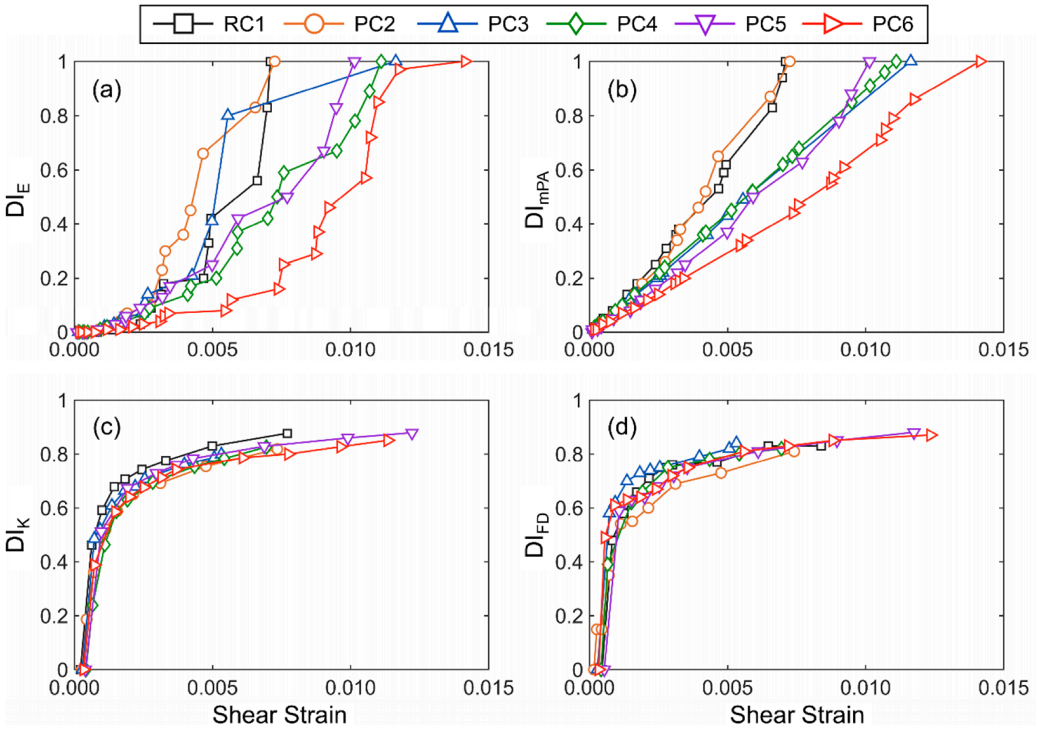

Figure 15. Damage curves of the RC beam–column joints evaluated using: (**a**) energy-based damage index, (**b**) modified Park–Ang damage index, (**c**) stiffness-based damage index, and (**d**) fractal-based damage index.

In contrast, the stiffness- and fractal-based damage curves differ substantially from the damage curves mentioned above (Figure 15c,d). The damage for these types of curves grows more rapidly at the initial loading stage, which corresponds to a shear strain level smaller than 0.002. Since the physical damage associated with this shear strain is primarily caused by minor crack growth, the stiffness- and fractal-based damage indices are both sensitive to the crack characteristics. The growth rate of damage decreases substantially as the damage index exceeds 0.6. In this loading stage, the damage curves are characterized by a flattened plateau until the damage indices reach 0.8~0.9 at the ultimate state. The slower rate of damage accumulation is attributed to the fact that the damage is sufficiently developed, and further loading may only slightly change the damage distribution under a large joint shear strain demand.

5.2. Correlation Between Fractal- and Stiffness-Based Damage

As discussed in the previous section, the fractal-based damage curves of the beam–column joints agree reasonably well with the stiffness-based counterparts. Figure 16 shows the scatter plot of the DI_{FD}-DI_K data points for all test specimens. Note that data points for different specimens are differentiated by color and marker shape. The black dashed line in the figure represents a ratio of 1:1 for the fractal- and stiffness-based damage indices. The results indicate that the distribution of the damage data appears to be highly uneven, since the majority of data points are located in the high-damage region ($DI_{FD} > 0.6$) but only a handful are in the low- and medium-damage region ($DI_{FD} \leq 0.6$). It is evident that the correlation between DI_{FD} and DI_K of data points with high level damage ($DI_{FD} > 0.6$) is notably superior to those with low- and medium-level damage. Additionally, DI_{FD} is consistently larger than DI_K for data associated with low- and medium-level damage ($DI_{FD} \leq 0.6$).

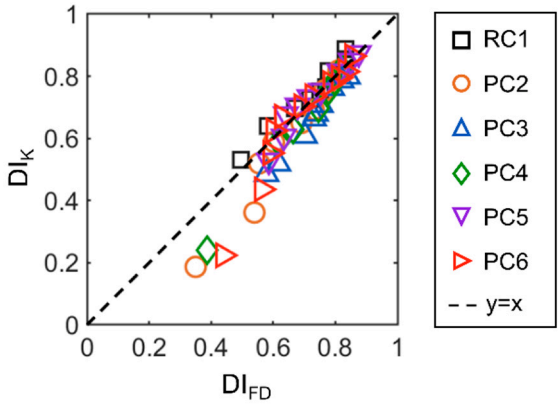

Figure 16. Comparison of the fractal- and stiffness-based damage indices of the RC joint specimens (notes: the black dashed line represents a ratio of 1:1 for the fractal- and stiffness-based damage indices).

To further evaluate the correlation between the fractal- and stiffness-based damage indices, the root-mean-square errors between the fractal- and stiffness-based damage indices $RMSE_{FD-K}$ for all beam–column joints are computed using the following equation:

$$RMSE_{FD-K} = \sqrt{\frac{\sum_{i=1}^{n}\left(DI_{FD}^{i} - DI_{K}^{i}\right)^{2}}{n}} \quad (12)$$

where n is the size of the dataset, DI_{FD}^{i} and DI_{K}^{i} are the fractal- and stiffness-based damage indices of an individual point in the dataset. Table 3 summarizes the root-mean-square errors of the fractal- and stiffness-based damage indices. It is noted that the RMSE of the damage indices for all specimens is reduced by 40% (from 0.064 to 0.036) by considering only the data points associated with high damage level ($DI_{FD} > 0.6$). The discrepancy of the damage indices remains no larger than 0.03 for all the specimens except PC3. The stiffness-based damage of specimen PC3 is consistently smaller than that of the fractal-based damage for data points with a high damage level, which is likely due to the overestimation of the joint stiffness at the reference (crack initiation) state. The validation against experimental data demonstrates that the fractal-based damage index effectively captures the stiffness deterioration of the RC beam–column joints, particularly for specimens under a high damage level (e.g., fully developed binary damage patterns).

Table 3. Root-mean-square errors between the fractal- and stiffness-based damage indices.

Specimen Name	RC1	PC2	PC3	PC4	PC5	PC6	All Specimens
$RMSE_{FD-K}$ (data for all damage levels)	0.034	0.089	0.067	0.063	0.027	0.078	0.064
$RMSE_{FD-K}$ (high damage level data only)	0.030	0.027	0.063	0.030	0.020	0.020	0.036

The fractal-based damage index (DI_{FD}) is a geometric feature extracted from binary images rather than a parameter derived from mechanical test data. Nevertheless, its strong correlation with the stiffness-based damage index (DI_K) is justified by the fact that the stiffness degradation physically arises from crack formation and propagation—mechanisms that simultaneously manifest as expanding or branching patterns in the binarized damage maps. The fractal dimension quantifies these morphological evolutions and encodes the progressive deterioration of the load-bearing behavior of the RC joints. Consequently, the

image-derived damage index (DI_{FD}) directly reflects the underlying mechanical behavior and justifies their use as a valid proxy for global stiffness loss (DI_K).

6. Conclusions

This study proposes an image-based methodology for quantitative damage assessment of reinforced concrete (RC) beam–column joints. The displacements and strain fields of the joints under seismic loads are extracted using speckle images captured by a stereo digital image correlation (DIC) system, and subsequently, fractal dimension analysis is introduced to evaluate the damage progression of the beam–column joints. The effectiveness of the proposed image-based damage analysis results is validated using quasi-static tests of six full-scale RC beam–column subassemblies. The effect of image processing parameters, namely, the concrete initial inelastic strain and binary damage threshold, on the damage assessment results is comprehensively explored. The damage assessment results obtained using the proposed image-based analysis procedures are presented and compared with mechanics-based damage metrics commonly found in the literature. Key findings regarding the image-based damage assessment of RC beam–column joints are summarized as follows:

1. Damage to the beam–column joints, as obtained using a strain-based damage pattern derived from the speckle images, is consistent with the crack patterns observed on the back side of the joints. This substantiates the use of strain-based damage patterns as an effective proxy for seismic damage of RC beam–column joints.
2. The fractal-based damage evolution of the beam–column joints correlates well with the stiffness deterioration. In both cases, damage to the joints increases rapidly in the early loading stage but grows at a slower rate as the damage index achieves ~0.6, which is characterized by the occurrence of sufficiently developed diagonal damage strips. Damage indices of the joints reach 0.8~0.9 at the peak strength state for both fractal- and stiffness-based damage assessment models.
3. The root-mean-square error between the fractal- and stiffness-based damage indices is sufficiently small (<0.4) in the case of high-level damage ($DI_{FD} > 0.6$). Due to the discrepancy associated with the damage initiation mechanism, the fractal-based damage is consistently larger than the stiffness-based counterpart in the early stage of loading ($DI_{FD} \leq 0.6$). In this regard, the fractal-based damage may only represent the upper bound value for estimating the early-stage stiffness deterioration of beam–column joints.
4. Although empirical parameters such as concrete inelastic strain and binary damage threshold are involved in the image-based damage analysis, the sensitivity study confirms that their effect on the damage assessment results is minimal (<2%) as long as they remain within the ranges as suggested by the study.

Combining DIC with fractal dimension analysis provides an effective solution for quantitatively assessing the seismic damage progression of RC beam–column joints via a non-contact monitoring strategy. This approach establishes a direct link between the local joint crack pattern and the stiffness degradation of RC beam–column joints by converting the strain-based damage maps into a fractal dimension index (DI_{FD}). Compared to the classical mechanics-based indices, the proposed fractal-based damage index is capable of capturing the spatial complexity and morphological evolution of cracks via a non-contact monitoring strategy. Further validation studies are strongly recommended to assess the applicability of the proposed image-based damage analysis procedures on a broader spectrum of RC beam–column joints (e.g., exterior configurations, those with high-strength concrete, etc.) and other RC elements (e.g., columns, walls).

Author Contributions: Conceptualization, Q.Z., X.W. and Z.C.; methodology, Q.Z.; validation, Q.Z.; data curation, Z.C. and B.C.; writing—original draft preparation, Q.Z. and X.W.; writing—review and editing, Q.Z., X.W., Z.C., B.C. and X.H.; visualization, Z.C. and B.C.; supervision, X.W. and X.H.; funding acquisition, X.W. and X.H. All authors have read and agreed to the published version of the manuscript.

Funding: This research is funded by the National Natural Science Foundation of China (Grant No.: 52378515), the Guangdong Basic and Applied Basic Research Foundation (Grant No.: 2022B1515250002), and the Key Research and Development Program of Guangzhou Municipal Science and Technology Bureau (Grant No.: 2025B03J0036).

Data Availability Statement: Data from this study are available from the corresponding author upon reasonable request.

Conflicts of Interest: The authors declare that they have no known competing financial interests or personal relationships that could appear to influence the work presented in this paper.

Abbreviations

The following abbreviations are used in this manuscript:

RC	Reinforced concrete
DIC	Digital image correlation
ROI	Region of interest

References

1. Sezen, H.; Whittaker, A.; Elwood, K.; Mosalam, K. Performance of reinforced concrete buildings during the August 17, 1999 Kocaeli, Turkey earthquake, and seismic design and construction practise in Turkey. *Eng. Struct.* **2003**, *25*, 103–114. [CrossRef]
2. Zhao, B.; Taucer, F.; Rossetto, T. Field investigation on the performance of building structures during the 12 May 2008 Wenchuan earthquake in China. *Eng. Struct.* **2009**, *31*, 1707–1723. [CrossRef]
3. Kam, W.Y.; Pampanin, S.; Elwood, K. Seismic performance of reinforced concrete buildings in the 22 February Christchurch (Lyttelton) earthquake. *Bull. N. Z. Soc. Earthq. Eng.* **2011**, *44*, 239–278. [CrossRef]
4. Kam, W.Y.; Pampanin, S.; Dhakal, R.; Gavin, H.P.; Roeder, C. Seismic performance of reinforced concrete buildings in the September 2010 Darfield (Canterbury) earthquake. *Bull. N. Z. Soc. Earthq. Eng.* **2010**, *43*, 340–350. [CrossRef]
5. Yurdakul, Ö.; Duran, B.; Tunaboyu, O.; Avşar, Ö. Field reconnaissance on seismic performance of RC buildings after the January 24, 2020 Elazığ-Sivrice earthquake. *Nat. Hazards* **2021**, *105*, 859–887.
6. Chang, B.; Hutchinson, T.C.; Wang, X.; Englekirk, R. Experimental seismic performance of beam-column subassemblies using ductile embeds. *J. Struct. Eng.* **2013**, *139*, 1555–1566. [CrossRef]
7. Chang, B.; Hutchinson, T.; Wang, X.; Englekirk, R. Seismic performance of beam-column subassemblies with high strength steel reinforcement. *ACI Struct. J.* **2014**, *111*, 1329–1338. [CrossRef]
8. Li, B.; Kulkarni, S.A. Seismic behavior of reinforced concrete exterior wide beam-column joints. *J. Struct. Eng.* **2010**, *136*, 26–36. [CrossRef]
9. Lin, C.M.; Restrepo, J.I. Seismic behaviour and design of reinforced concrete interior beam-column joints. *Bull. N. Z. Soc. Earthq. Eng.* **2002**, *35*, 108–128. [CrossRef]
10. Abdel-Qader, I.; Abudayyeh, O.; Kelly, M.E. Analysis of edge-detection techniques for crack identification in bridges. *J. Comput. Civ. Eng.* **2003**, *17*, 255–263. [CrossRef]
11. Hutchinson, T.C.; Chen, Z. Improved image analysis for evaluating concrete damage. *J. Comput. Civ. Eng.* **2006**, *20*, 210–216. [CrossRef]
12. Lattanzi, D.; Miller, G.R. Robust automated concrete damage detection algorithms for field applications. *J. Comput. Civ. Eng.* **2014**, *28*, 253–262. [CrossRef]
13. Paal, S.G.; Jeon, J.S.; Brilakis, I.; DesRoches, R. Automated damage index estimation of reinforced concrete columns for post-earthquake evaluations. *J. Struct. Eng.* **2015**, *141*, 04014228. [CrossRef]
14. Cha, Y.J.; Choi, W.; Büyüköztürk, O. Deep learning-based crack damage detection using convolutional neural networks. *Comput.-Aided Civ. Infrastruct. Eng.* **2017**, *32*, 361–378.
15. Dung, C.V. Autonomous concrete crack detection using deep fully convolutional neural network. *Autom. Constr.* **2019**, *99*, 52–58. [CrossRef]

16. Gao, Y.; Mosalam, K.M. Deep transfer learning for image-based structural damage recognition. *Comput.-Aided Civ. Infrastruct. Eng.* **2018**, *33*, 748–768.
17. Liang, X. Image-based post-disaster inspection of reinforced concrete bridge systems using deep learning with Bayesian optimization. *Comput.-Aided Civ. Infrastruct. Eng.* **2019**, *34*, 415–430.
18. Pan, B. Digital image correlation for surface deformation measurement: Historical developments, recent advances and future goals. *Meas. Sci. Technol.* **2018**, *29*, 082001. [CrossRef]
19. Huang, H.W.; Li, Q.T.; Zhang, D.M. Deep learning based image recognition for crack and leakage defects of metro shield tunnel. *Tunn. Undergr. Space Technol.* **2018**, *77*, 166–176. [CrossRef]
20. Kim, H.; Ahn, E.; Shin, M.; Sim, S.H. Crack and noncrack classification from concrete surface images using machine learning. *Struct. Health Monit.* **2019**, *18*, 725–738.
21. Hou, S.; Dong, B.; Wang, H.; Wu, G. Inspection of surface defects on stay cables using a robot and transfer learning. *Autom. Constr.* **2020**, *119*, 103382. [CrossRef]
22. Corr, D.; Accardi, M.; Graham-Brady, L.; Shah, S. Digital image correlation analysis of interfacial debonding properties and fracture behavior in concrete. *Eng. Fract. Mech.* **2007**, *74*, 109–121. [CrossRef]
23. Gencturk, B.; Hossain, K.; Kapadia, A.; Labib, E.; Mo, Y.L. Use of digital image correlation technique in full-scale testing of prestressed concrete structures. *Measurement* **2014**, *47*, 505–515. [CrossRef]
24. Mahal, M.; Blanksvärd, T.; Täljsten, B.; Sas, G. Using digital image correlation to evaluate fatigue behavior of strengthened reinforced concrete beams. *Eng. Struct.* **2015**, *105*, 277–288. [CrossRef]
25. Destrebecq, J.F.; Toussaint, E.; Ferrier, E. Analysis of cracks and deformations in a full scale reinforced concrete beam using a digital image correlation technique. *Exp. Mech.* **2011**, *51*, 879–890.
26. Gehri, N.; Mata-Falcón, J.; Kaufmann, W. Automated crack detection and measurement based on digital image correlation. *Constr. Build. Mater.* **2020**, *256*, 119383. [CrossRef]
27. Gehri, N.; Mata-Falcón, J.; Kaufmann, W. Refined extraction of crack characteristics in large-scale concrete experiments based on digital image correlation. *Eng. Struct.* **2022**, *251*, 113486. [CrossRef]
28. Sarkar, N.; Chaudhuri, B.B. An efficient differential box-counting approach to compute fractal dimension of image. *IEEE Trans. Syst. Man Cybern.* **1994**, *24*, 115–120. [CrossRef]
29. Carrillo, J.; Avila, W. Assessment of seismic damage of thin and lightly reinforced concrete walls using fractal dimension of cracking. *Earthq. Eng. Struct. Dyn.* **2017**, *46*, 661–675.
30. Carrillo, J.; Dominguez, D.; Prado, N. Seismic damage index based on fractal dimension of cracking on thin reinforced concrete walls. *ACI Struct. J.* **2017**, *114*, 1649–1658. [CrossRef]
31. Woods, J.E.; Yang, Y.S.; Chen, P.C.; Lau, D.T.; Erochko, J. Automated crack detection and damage index calculation for RC structures using image analysis and fractal dimension. *J. Struct. Eng.* **2021**, *147*, 04021019. [CrossRef]
32. Grassl, P.; Jirásek, M. Damage-plastic model for concrete failure. *Int. J. Solids Struct.* **2006**, *43*, 7166–7196. [CrossRef]
33. Correlated Solutions Inc. *Vic-3D 9 Manual and Testing Guide*; Correlated Solutions Inc.: Irmo, SC, USA, 2025. Available online: https://correlated.kayako.com/section/9-manuals-and-guides (accessed on 6 November 2024).
34. MathWorks. *Computer Vision Toolbox*; MathWorks: Natick, MA, USA, 2025. Available online: https://www.mathworks.com/help/vision/ (accessed on 17 November 2024).
35. Sun, Y.; Pang, J.H. Study of optimal subset size in digital image correlation of speckle pattern images. *Opt. Lasers Eng.* **2007**, *45*, 967–974. [CrossRef]
36. Dong, Y.; Pan, B. A review of speckle pattern fabrication and assessment for digital image correlation. *Exp. Mech.* **2017**, *57*, 1161–1181. [CrossRef]
37. Pan, B.; Qian, K.; Xie, H.; Asundi, A. Two-dimensional digital image correlation for in-plane displacement and strain measurement: A review. *Meas. Sci. Technol.* **2009**, *20*, 062001. [CrossRef]
38. Seemab, F.; Schmidt, M.; Baktheer, A.; Classen, M.; Chudoba, R. Automated detection of propagating cracks in RC beams without shear reinforcement based on DIC-controlled modeling of damage localization. *Eng. Struct.* **2023**, *286*, 116118. [CrossRef]
39. Mandelbrot, B.B. Self-affine fractals and fractal dimension. *Phys. Scr.* **1985**, *32*, 257. [CrossRef]
40. Wang, L.; Wang, Z.; Xie, W.; Song, X. Fractal study on collective evolution of short fatigue cracks under complex stress conditions. *Int. J. Fatigue* **2012**, *45*, 1–7. [CrossRef]
41. Farhidzadeh, A.; Dehghan-Niri, E.; Moustafa, A.; Salamone, S.; Whittaker, A. Damage Assessment of Reinforced Concrete Structures Using Fractal Analysis of Residual Crack Patterns. *Exp. Mech.* **2013**, *53*, 1607–1619. [CrossRef]
42. Chen, Z.Y.; Han, X.L.; Wang, X.; Cui, B.; Huang, G.-X.; Li, Z.-C.; Ji, J. Seismic behavior of precast concrete beam-column subassemblies with joint rebar couplers. *Structures* **2025**, *79*, 109553. [CrossRef]
43. *JGJ/T101-2015*; Specification for the Seismic Test of Buildings. China Architecture and Building Press: Beijing, China, 2015.
44. Williams, M.S.; Sexsmith, R.G. Seismic damage indices for concrete structures: A state-of-the-art review. *Earthq. Spectra* **1995**, *11*, 319–349.

45. Banon, H.; Veneziano, D. Seismic safety of reinforced concrete members and structures. *Earthq. Eng. Struct. Dyn.* **1982**, *10*, 179–193. [CrossRef]
46. Mahin, S.A.; Bertero, V.V. An evaluation of inelastic seismic design spectra. *J. Struct. Div.* **1981**, *107*, 1777–1795. [CrossRef]
47. Park, Y.J.; Ang, H.S. Mechanistic seismic damage model for reinforced concrete. *J. Struct. Eng.* **1985**, *111*, 722–739. [CrossRef]
48. Dong, J.; Bai, Y.; Liu, Y.; Cong, X.; Shen, C. Seismic damage assessment of new type prefabricated concrete frame joints. *J. Constr. Steel Res.* **2024**, *215*, 108553. [CrossRef]

Disclaimer/Publisher's Note: The statements, opinions and data contained in all publications are solely those of the individual author(s) and contributor(s) and not of MDPI and/or the editor(s). MDPI and/or the editor(s) disclaim responsibility for any injury to people or property resulting from any ideas, methods, instructions or products referred to in the content.